

Brownian spin-locking effect

Received: 10 December 2024

Accepted: 17 October 2025

Published online: 18 November 2025

 Check for updatesXiao Zhang^{1,7}, Peiyang Chen^{1,2,7}, Mei Li¹, Yuzhi Shi³, Erez Hasman⁴,
Bo Wang¹ & Xianfeng Chen^{1,5,6}

Brownian systems are characterized by spatiotemporal disorder, which arises from the erratic motion of particles driven by thermal fluctuations. When light interacts with such systems, it typically produces unpolarized and uncorrelated fields. Here we report the observation of a large-scale spin-locking effect of light within a Brownian medium. In an observation direction perpendicular to the incident wave's momentum, scattering naturally divides into two diffusion regions, each associated with an opposite spin from the Brownian nanoparticles. This effect arises from the intrinsic spin-orbit interactions of scattering from individual nanoparticles, which ubiquitously generate radiative spin fields that propagate through the Brownian medium with multiple incoherent scattering. It offers an experimental platform for exploring macroscale spin behaviour of diffused light, with potential applications in precision metrology for measuring various nanoparticle properties. Our findings may inspire the study of analogous phenomena for different waves from unusual spin-orbit interactions in complex disordered systems.

The study of coherent wave interactions with complex disordered structures has led to many unique wave phenomena, including Anderson localization^{1,2}, super oscillation³, branched flow⁴ and Hall effects⁵. Spin is an intrinsic angular momentum carried by different waves. It plays a central role in both classical and quantum phenomena and has broad implications in various branches of physics. In condensed matter physics, spin interactions give rise to exotic states of matter, such as topological insulators^{6,7} and spin liquids^{8,9}, while magnetic properties emerge due to the coupling of spin and orbital degrees of freedom¹⁰. In optics, spin angular momentum is associated with light's circular polarization^{11,12}. The interplay between light and matter gives rise to many optical spin-dependent effects, such as the Rashba effect^{13,14}, spin Hall effect¹⁵, universal spin-momentum locking of evanescent waves^{16–20}, and exotic spin and momentum structures in optical fields^{21–24}. Many spin-dependent phenomena are described as a stable separation between two spin components of light, which can be characterized by a geometric-phase gradient $\partial\Phi_c/\partial\xi$ that occurs

in a general parameter space ξ , driven by various spin-orbit interactions (SOIs)²⁵. Generally, $\partial\Phi_c/\partial\xi$ arises from spatially asymmetric light-matter interactions that are induced either by asymmetric optical illuminations^{26,27} or by engineered structures^{28–30}. However, coherent waves can severely destroy SOI due to overwhelming randomness. As the scale of disorder increases, a delicate symmetry-breaking condition becomes less defined, eliminating spin-split phenomena as $\langle\partial\Phi_c/\partial\xi\rangle$ approaches zero^{31,32}.

Compared with static disordered structures, a Brownian system is not only spatially disordered but also temporally fluctuating. Brownian motion exists widely in nature. It is not only a cornerstone of statistical physics³³, but also a key component in numerous practical applications across a wide range of research fields including chemistry, biology and even finance. In optics, the diffusion properties of Brownian particles give rise to an optical technique for measuring the size of nanoparticles, known as dynamic light scattering (DLS)³⁴. For colloidal suspensions, the random movement of particles results from their

¹State Key Laboratory of Photonics and Communications, School of Physics and Astronomy, Shanghai Jiao Tong University, Shanghai, China.

²Zhiyuan College, Shanghai Jiao Tong University, Shanghai, China. ³Institute of Precision Optical Engineering, School of Physics Science and Engineering, Tongji University, Shanghai, China. ⁴Atomic-Scale Photonics Laboratory, Russell Berrie Nanotechnology Institute, and Helen Diller Quantum Center, Technion – Israel Institute of Technology, Haifa, Israel. ⁵Shanghai Research Center for Quantum Sciences, Shanghai, China. ⁶Collaborative Innovation Center of Light Manipulations and Applications, Shandong Normal University, Jinan, China. ⁷These authors contributed equally: Xiao Zhang, Peiyang Chen.

✉ e-mail: mehasman@technion.ac.il; wangbo89@sjtu.edu.cn; xfchen@sjtu.edu.cn

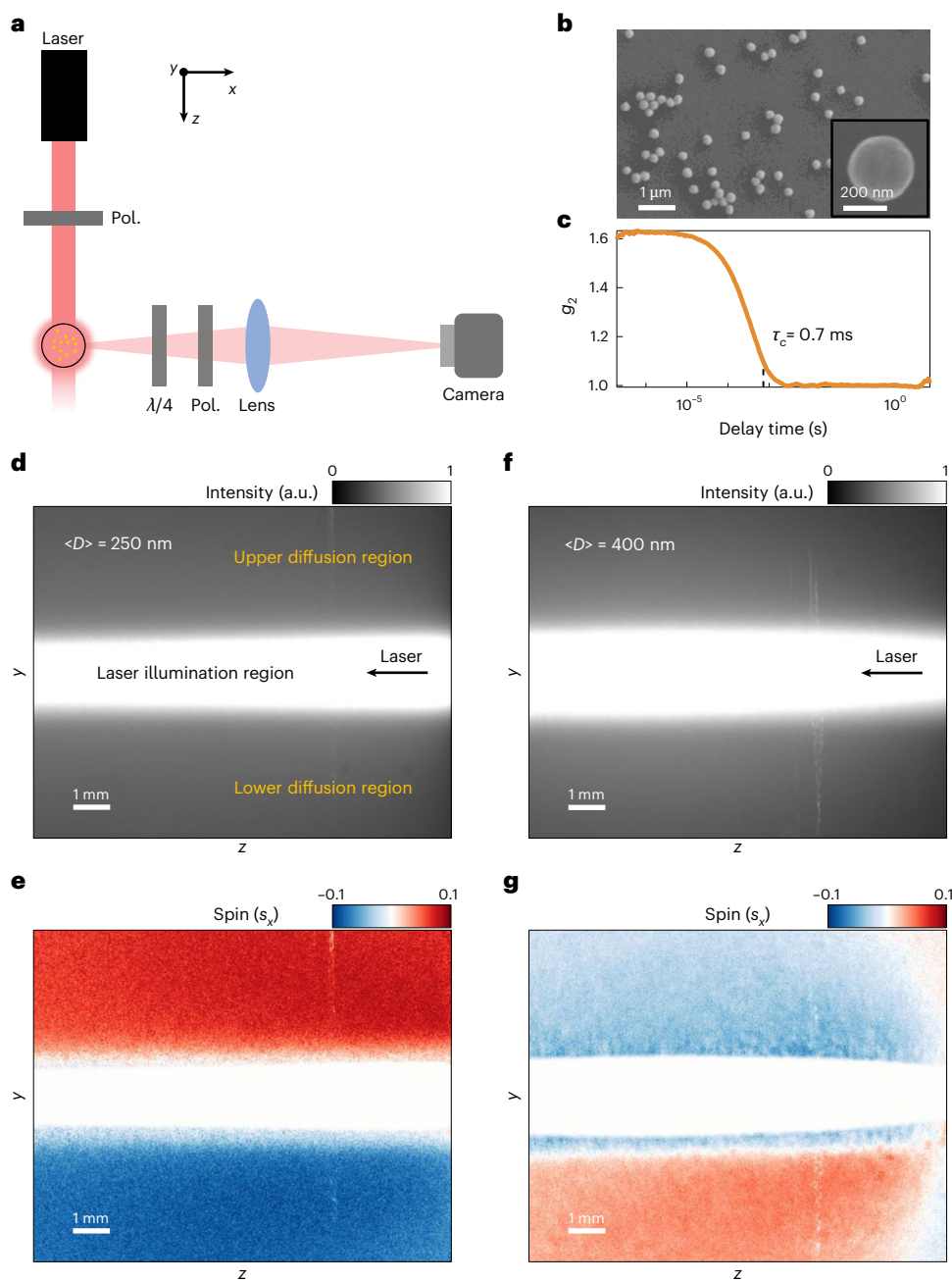


Fig. 1 | Experimental observation of the Brownian spin-locking effect of light scattered from Brownian nanoparticles. **a**, Experimental set-up for observing the effect. A linearly polarized laser (639 nm) impinges on the sample at normal incidence. The sample is contained in a glass vial with AuNPs suspended in water. The observation path is set at a scattering angle perpendicular to the incident light. The images are captured by the camera using a single lens. Pol., linear

polarizer; QWP, quarter-wave plate; Lens, convex lens ($f = 80\text{ mm}$). **b**, An example of a scanning electron microscope image of the AuNPs with $\langle D \rangle = 250\text{ nm}$. **c**, Measured second-order autocorrelation function of the AuNPs using a DLS instrument. The coherence time is $\tau_c \approx 0.7\text{ ms}$. **d, e**, Intensity (**d**) and spin (**e**) distributions of light scattered from AuNPs ($\langle D \rangle = 250\text{ nm}$). **f, g**, Intensity (**f**) and spin (**g**) distributions of light scattered from AuNPs ($\langle D \rangle = 400\text{ nm}$).

stochastic collisions with fluid molecules. Therefore, the locations of these Brownian particles are unpredictable, and the mean squared displacement of these particles is proportional to time.

Here, we report an unforeseen Brownian spin-locking effect, manifested as a stable spatial distribution of spin-polarized light regardless of the Brownian motion of the scattered nanoparticles. This phenomenon arises from the spatiotemporally disordered scattering from a massive number of spherical nanoparticles in the colloidal suspension. Instead of being destroyed by strong and dynamic disorder, the spin fields are divided into two opposite macroscale regions with a stable and homogeneous spatial distribution. Its physical mechanism is composed of

two aspects: one is the intrinsic SOI from nanoparticles, and the other is the incoherent multiple scattering among them. First, spin-symmetry breaking emerges in an observation direction perpendicular to the incident momentum. This is a universal effect for optical scattering that does not require any structural anisotropy or chirality. Specifically, it can emerge for isotropic spherical nanoparticles excited by linearly polarized plane waves. The scattered spin is generally partially aligned with the kinetic momentum (that is, Poynting vector). It can be characterized by a power-law decaying function ($\propto 1/r^2$) and radiates into the far field, leading to multiple scattering. Second, the erratic movement of many nanoparticles leads to continuous density variation and incoherent multiple

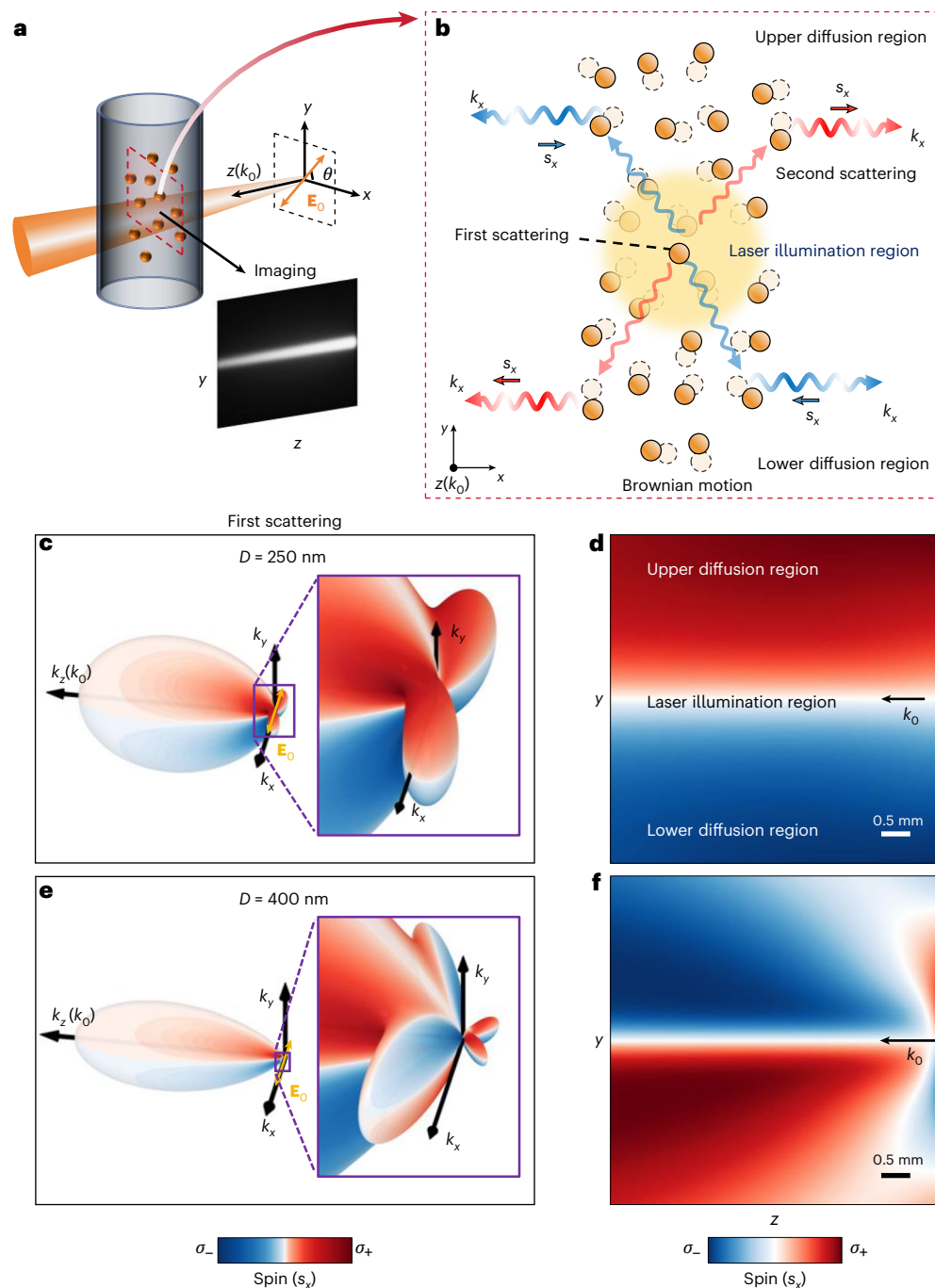


Fig. 2 | The two-step scattering theory for the spin-locking effect. **a**, Schematic diagram of the observation system. **b**, The working principle in the xy plane. In the laser illumination region, the incident laser excites one of the nanoparticles, resulting in a radiation source \mathbf{E}_b . \mathbf{E}_b propagates into the diffusion region with direction-dependent spin and momentum, and excites another nanoparticle, that is, the second scattering. The imaging system then captures the polarized field from the incoherent summation (because of the Brownian motion) of many

second scatterings from the k_x direction. **c,e**, The theoretical kinetic momenta and spin distributions of a single AuNP with $D = 250$ nm (**c**) and $D = 400$ nm (**e**). The nanoparticles are excited by \mathbf{E}_0 at a wavelength of 639 nm. The radial distance from each point on the surface to the origin represents the magnitude of the normalized kinetic momentum. The blue and red colours represent the projection of the far-field spin onto the k_x direction. **d,f**, The calculated spatial distributions of spin from the incoherent scattering theory for AuNPs $D = 250$ nm (**d**) and $D = 400$ nm (**f**).

scattering. Thermodynamic disorder preserves the spin distribution of a single nanoparticle, and it notably reduces the destructive interference and spin fluctuations that usually occur in coherent disordered system. Because of this dynamic disorder, the spin field is continuously accumulated through multiple Brownian nanoparticles, resulting in distinct spin fields homogeneously distributed on opposite sides of the laser beam. Notably, the experimentally observed spin split can easily reach a centimetre scale, which is so far the largest reported in disordered structures.

Typical experimental results

The experimental setting for observing the spin-locking effect is shown in Fig. 1a. The sample is placed in a glass container, which consists of spherical gold nanoparticles (AuNPs) suspended in water (Supplementary Section 7). The average diameter of AuNPs is $\langle D \rangle = 250$ nm (Fig. 1b). To observe the scattering effect, an x -polarized plane wave laser (wavelength 639 nm, beam width ~ 2 mm) impinges on the sample at a normal incidence angle. The observation path is positioned perpendicular to

the incident direction, and we used a simple lens system to capture the scattering images with the camera. A quarter-wave plate and a post-polarizer are used to detect the intensities of opposite spin polarizations. All experiments are performed at room temperature ($\sim 25^\circ\text{C}$), at which we characterized the Brownian motion behaviour of the samples using a DLS method (Supplementary Section 11). As shown in Fig. 1c, the second-order autocorrelation function g_2 indicates a strong intensity fluctuation of the scattered light on timescales above $\tau_c = 0.7$ ms. The acquisition time of our detector system is about 2 s; hence the observations are performed in the incoherent region. Typical examples of the observed intensity and spin distributions are shown in Fig. 1d and Fig. 1e, respectively. The scattering intensity distribution consists of a region that spatially overlaps with the laser beam and two diffusion regions on opposite sides of the beam. The upper and lower diffusion regions show opposite spin angular momenta, respectively. Here, the spin (normalized) is characterized by $s_x = (I_R - I_L)/(I_R + I_L)$, with $I_{R,L}$ being the intensities for right- and left-handed circular polarizations. Despite the thermodynamic nature of the system, the observed spin split is very large and robust. Each spin region reaches a centimetre scale, and the spatial spin fluctuation in each region is very small (Fig. 3c and Fig. 3d, bottom right). Apparently, this unusual spin phenomenon is neither due to tilted optical illumination nor to the transverse spin of the laser^{35,36}, because we used a normally incident plane wave as the excitation (Gaussian beam with a ~ 2 -mm beam waist; Extended Data Fig. 1). This spin effect potentially comes from the colloid. As a simple verification, we performed another experiment with the same optical setting but using a bottle of different AuNPs with $\langle D \rangle = 400$ nm. As shown in Fig. 1f,g, the sign of spin is flipped. Therefore, this indicates that the physical properties of the Brownian scattering system play a critical role in the spin-momentum locking effect. This phenomenon is also demonstrated for nanoparticles of different materials and concentration (Extended Data Fig. 2 and Supplementary Section 11).

A two-step incoherent scattering theory

To evaluate the observed phenomena from a macroscale scattering system, we established a theory that simplifies the complex scattering into a few essential steps (Fig. 2a,b). We calculated a two-step scattering process for a combination of any two nanoparticles: one is located in the illumination region (for the first scattering) and the other in the diffusion region (for the second scattering). The incident laser field, \mathbf{E}_0 , excites one of the nanoparticles in the illumination region, resulting in $\mathbf{E}_b = \mathbf{M} \times \mathbf{E}_0$. Here, \mathbf{M} represents the Mie scattering matrix and \mathbf{E}_b propagates in space following the exact solution (Methods, Extended Data Fig. 3 and Supplementary Section 8). As depicted in Fig. 2c, the far-field distributions of spin and kinetic momentum exhibit distinct angular features around the first scattering nanoparticle, depending on the radiation direction \mathbf{k} (k_x, k_y, k_z). The radial distance from each point on the surface to the origin represents the magnitude of the normalized kinetic momentum, indicating that \mathbf{E}_b radiates an electromagnetic field with a strongly directional momentum pattern. The surface is colour-mapped according to the projection of the far-field spin onto the k_x direction, which corresponds to our experimentally observed s_x , revealing a non-trivial spin structure in the electromagnetic field. The spin field propagates to the diffusion region and excites another nanoparticle to induce a second scattering. The polarized light in the diffusion regions is obtained from many incoherent second scatterings with varying positions of nanoparticles.

The directional properties of the kinetic momentum and the spin of the first scattering are crucial for observing the macroscale spin-locking effect. Taking Fig. 2c as an example (AuNP, $D = 250$ nm), in the k_x - k_y plane, the AuNP radiates spin-up ($s_x > 0, \sigma_+$) polarization to the region of $k_y > 0$, and spin-down ($s_x < 0, \sigma_-$) polarization to the region of $k_y < 0$. This spin symmetry breaking is a typical result of the interaction between \mathbf{E}_0 and a nanoparticle, which radiates an electromagnetic field beyond the electric dipole approximation. In the k_y - k_z plane, spin

splits along the k_y direction, and two asymmetric lobes emerge (Fig. 2c, inset). Therefore, after performing many incoherent secondary scatterings, we can see opposite spin polarizations in the two diffusion regions (Fig. 2d), which is in good agreement with our experimental observation (Fig. 1e).

When the size of nanoparticle increases, the kinetic momentum and spin structures will both change and even become complex, due to the increased multipole components in Mie scattering. For an AuNP with $D = 400$ nm, we see an opposite spin pattern in the k_x - k_y plane, in comparison with that from $D = 250$ nm, and there are six spin lobes in the k_y - k_z plane (Fig. 2e, inset). These properties eventually result in a flipped spin distribution in the diffusion regions with small side lobes near the laser's side, as shown in Fig. 2f. This theoretical result also agrees well with our experimental observation (Fig. 1g).

We emphasize that the spin structures in Fig. 2c,e originate from the non-diagonal components of \mathbf{M} , indicating a universal SOI effect when we convert a two-dimensional-vector electromagnetic field into three dimensions via scattering. For extremely small particles in the Rayleigh limit, \mathbf{M} is Green's function operator. In our experiments, the size of the nanoparticles is large enough to violate Rayleigh approximation, and multipole response inevitably occurs. The scattered spin fields become longitudinal and partially aligned with the kinetic momentum. Thus, the spin field can propagate to the diffusion regions for second and multiple scattering.

The role of Brownian motion in the spin-locking effects

To clearly show the role of the Brownian motion in these effects, we performed additional experiments to detect the spatial distribution of the spin fields as a function of the camera's acquisition time (t_{exp}). To do this, we utilized a polarized grating that spatially separates the spin-up and spin-down components, projecting them onto different regions of the camera for simultaneous detection (Fig. 3a). Figure 3c shows the experimental obtained g_2 of sample A (Fe_3O_4 , $\langle D \rangle = 470$ nm; Fig. 3b, left). The coherent time, $\tau_c \approx 2.4$ ms, characterizes the Brownian motion diffusive velocity of the nanoparticles. By controlling the acquisition time of the camera from $t_{\text{exp}} = 0.43$ ms to 200 ms, we captured the spin distributions in the upper and lower diffusion regions and analysed their average spin values $\langle s_x \rangle$ and spatial fluctuations Δs_x (Fig. 3c). For $t_{\text{exp}} \ll \tau_c$, namely, a very short acquisition time, the colloidal system can be considered static, so that the interferences between scatterings are coherent. In this case, we observe a strong spatial fluctuation of the spin across each diffusion region, distributing as a Gaussian profile with a width $\Delta s_x \approx 0.21$. The average spin values for the upper and lower diffusion regions are $\langle s_x \rangle_{\text{up}} \approx -0.07$ and $\langle s_x \rangle_{\text{low}} \approx 0.05$, respectively. Clearly, we have $\Delta s_x \approx 2|\langle s_x \rangle_{\text{up}} - \langle s_x \rangle_{\text{low}}|$, and the spin is not 'locked' in the diffusion regions because of the strong fluctuation Δs_x . For $t_{\text{exp}} \approx \tau_c$, the width of spin distribution notably decreases, and we obtain $\Delta s_x \approx |\langle s_x \rangle_{\text{up}} - \langle s_x \rangle_{\text{low}}|$. This is a spin-locking criterion determined by the coherent time of the Brownian motion. For $t_{\text{exp}} \gg \tau_c$, which returns to the dynamical limit with sufficiently long Brownian motions, we have $\Delta s_x \ll |\langle s_x \rangle_{\text{up}} - \langle s_x \rangle_{\text{low}}|$, and two homogeneous spin distributions are observed in the two diffusion regions. Notably, the average values $\langle s_x \rangle$ are stable while we change t_{exp} , and only the fluctuation Δs_x is affected by the Brownian motion. To validate our analysis, we performed another group of experiments with sample B that consists of nanoparticles with a different material and size (SiO_2 , $\langle D \rangle = 1.69$ μm , Fig. 3b, right). We observed similar behaviours of the Δs_x and $\langle s_x \rangle$ as a function of t_{exp} , and again, $\Delta s_x \approx |\langle s_x \rangle_{\text{up}} - \langle s_x \rangle_{\text{low}}|$ at $t_{\text{exp}} \approx \tau_c$ (Fig. 3d). In theory, we also show a similar evolution of Δs_x and $\langle s_x \rangle$ by continually changing the degree of coherence in the scattering system, verifying our experimental observations (Extended Data Fig. 4 and Supplementary Section 13).

Results from different incident polarizations

From Fig. 2c,e, we see that the radiation momentum and spin of the first scattering are associated with the incident polarization \mathbf{E}_0 . Therefore,

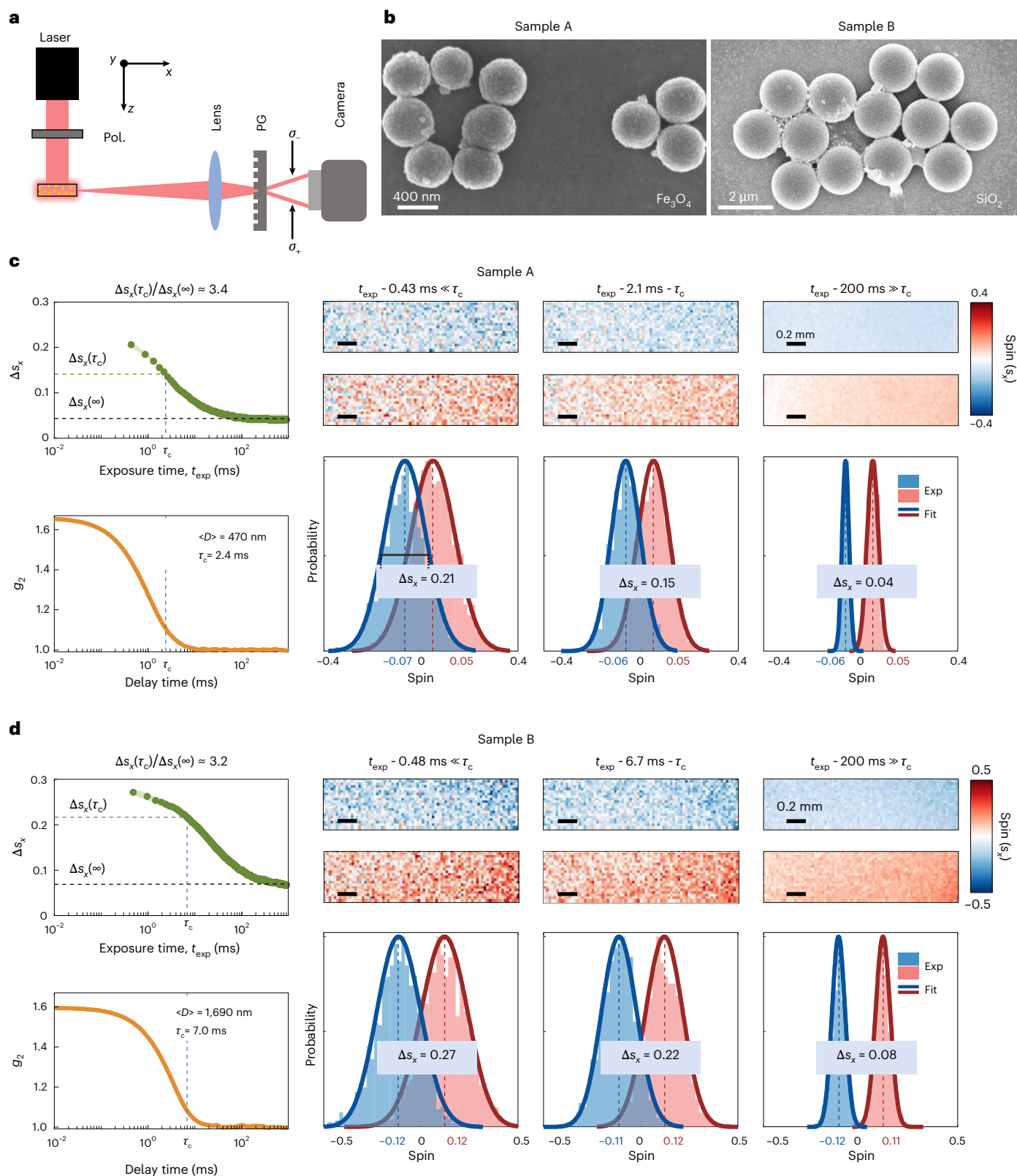


Fig. 3 | Measuring the Brownian spin-locking effect with different camera acquisition times. **a**, Schematic of the optical setup. Laser wavelength: 639 nm. Pol., linear polarizer; Lens, focal length 80 mm; PG, polarized grating. **b**, SEM images of two samples: the Fe_3O_4 nanoparticles with $\langle D \rangle = 470$ nm and the SiO_2 nanoparticles with $\langle D \rangle = 1,690$ nm, respectively. **c, d**, The experimental results of samples A (**c**) and B (**d**). The measured spatial spin distribution width is plotted as a function of acquisition time t_{exp} (green dots). The second-order autocorrelation

function of intensity (g_2) was measured using a DLS device (orange curves). The images are spatial spin distributions in the upper and lower diffusion regions, taken at different t_{exp} . The histograms (Exp) present the experimentally measured spatial spin statistics from the corresponding upper and lower diffusion regions, and the solid curves (Fit) represent the numerical fits using a Beta distribution. The vertical dashed lines and the coloured labels in the spin distribution plots denote the averaged spin values for the upper and lower diffusion regions.

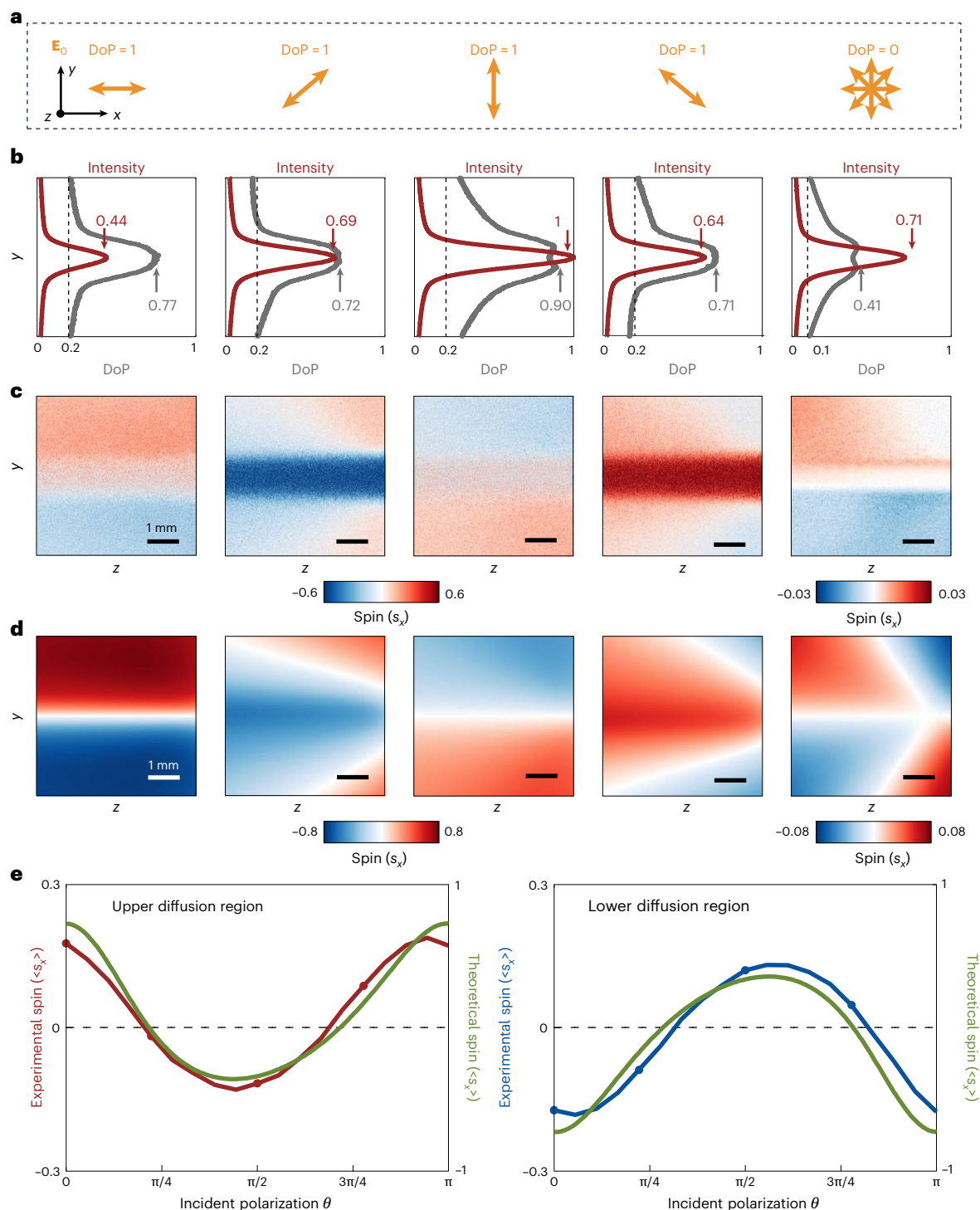


Fig. 4 | The macroscale spin effects for different incident polarizations. **a**, Example sketches of several incident polarizations. The DoPs for the linear polarizations are 1, while that of the unpolarized light is 0. The measured sample is a colloid of AuNPs with $\langle D \rangle = 200$ nm. **b**, Experimental results of the scattering intensity (red curves) and the DoP (grey curves) along the y axis. **c**, Experimentally observed spin distributions for different incident polarizations.

d, Theoretical spin distributions for different incident polarizations. The nanoparticles in theory are gold nanospheres with $D = 200$ nm, excited by light at the wavelength of 639 nm. **e**, Experimental (red and blue curves) and theoretical (green curves) spin for different incident linear polarizations. The curves are the averaged results over the entire upper or lower diffusion regions.

these momentum and spin structures will rotate along with \mathbf{E}_0 . To study this, we performed experiments with different linear polarizations characterized by an incident polarization angle θ (Figs. 2a and 4a). The Stokes parameters (s_1, s_2, s_3 and s_0) are measured for both the incident laser and the scattered light to characterize the polarization states and the degree of polarization (DoP) (Methods). As shown in Fig. 4b, we depicted the

average intensity distribution (s_0) and the DoP of the image along the y direction for several different incident polarizations. The illumination region and diffusion region are distinguished by the drastically different scattering intensity and DoP. Generally, illumination region remains a relatively high DoP, as it is dominated by the first scattering process, consistent with our assumption. In particular, for the y-polarization

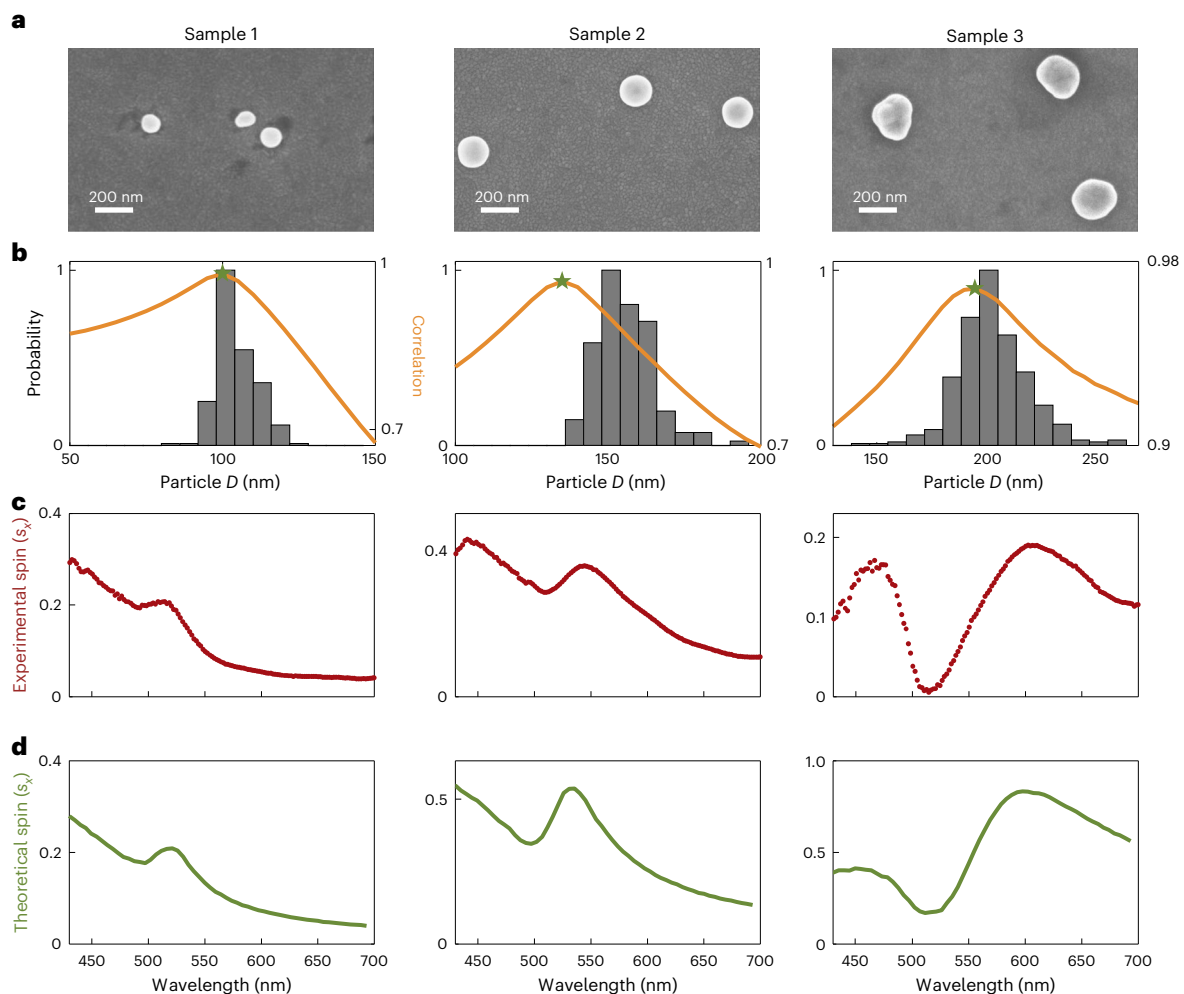


Fig. 5 | Spin-resolved spectroscopy of the Brownian spin-locking effect for measuring the size of AuNPs. **a**, Typical SEM images of three different samples, with their nominal $\langle D \rangle = 100$ nm, 150 nm and 200 nm, respectively. **b**, The histograms are measured D distributions of the three samples using SEM images. The curves are correlation functions defined by the overlap between $s_{x,\text{theory}}(D, \lambda)$ and $s_x(\lambda)$, which is observed in the spin-resolved spectroscopy. The SEM-obtained

highest probability regions are 98–104 nm, 148–154 nm and 197–205 nm, respectively. The highest correlations (marked as stars) obtained from the spin-resolved spectroscopy are 100 nm, 135 nm and 195 nm, respectively. **c**, Experimentally observed $s_x(\lambda)$ from spin-resolved spectroscopy. **d**, Examples of the theoretical spin-resolved spectra calculated using $D = 100$ nm, $D = 135$ nm and $D = 195$ nm, corresponding to the highest correlations in **b**.

($\theta = \pi/2$), the DoP in the illumination region can even reach 0.9 (Fig. 4b, middle), meaning that the y -polarization is hardly affected by the random system. In general, the DoP in the diffusion regions is much lower (0.1–0.2), attributed to many incoherent secondary and multiple scatterings. Therefore, the experimentally observed small s_x in the diffusion region is due not only to the elliptical polarization, but also to the depolarization effect. In total, we performed experiments with 19 different incident polarizations (from $\theta = 0$ to π) (Fig. 4e). The measured $\langle s_x \rangle$ in the upper and lower diffusion regions agrees well with our incoherent scattering theory (Fig. 4e). Example comparisons between experimental and theoretical spin distributions are depicted in Fig. 4c,d.

Furthermore, we investigated the ‘locking’ effect from unpolarized laser illumination. The unpolarized light was created by continually rotating the incident polarization spanning 180°, and then we measured the Stokes parameters of the scattered light. In this case, the DoP of the incident light is 0. However, the DoP of the scattered light remains 0.41 in the illumination region and 0.1 in the diffusion regions, showing polarized scattered fields from unpolarized illumination. Moreover, we observed a clear spin-locking effect with smaller $\langle s_x \rangle$ (Fig. 4c,d, rightmost panels), indicating the robustness of the spin-locking effect under the randomness of incident polarization.

Spin-resolved spectroscopy for nanoparticle size measurement

The spin-resolved optical field carries information about individual nanoparticles through multiple scattering, which allows us to detect the physical properties of Brownian nanoparticles from a paraxial optical imaging system. As a proof of concept, we developed spin-resolved optical spectroscopy to measure the size of the AuNPs. To do this, we utilized a broadband laser as the excitation source, and the camera was replaced by a spectrometer, which captured $s_x(\lambda)$ (Supplementary Section 12). We prepared three AuNP samples with different nominal $\langle D \rangle$ (typical scanning electron microscopy (SEM) images are shown in Fig. 5a), and we used SEM to measure their size distributions as a benchmark reference (Fig. 5b, histograms). The experimentally observed spin-spectra $s_x(\lambda)$ are shown in Fig. 5c, in the wavelength range between 430 nm and 700 nm. The experimental $s_x(\lambda)$ is compared with different theoretical spectra, $s_{x,\text{theory}}(D, \lambda)$, which are calculated using the incoherent scattering theory applied to many AuNPs with size D (Fig. 5d). The normalized correlations between $s_x(\lambda)$ and $s_{x,\text{theory}}(D, \lambda)$ are depicted as orange curves in Fig. 5b, and the stars mark the highest correlation for each sample. We see a good agreement between our method and the SEM measurements. In particular, for sample 1, the highest correlation

occurs at $D = 100$ nm, while the value obtained from SEM is 101 nm. The accuracy of our spin-resolved spectroscopy is 99%. For samples 2 and 3, the accuracy is 89% and 97%, respectively. The precision can be further improved by increasing the detection wavelength range, or using a feedback algorithm for optimization.

Discussion

In summary, we have observed a spin-locking phenomenon of light from a Brownian system with spatiotemporal disorder. The system consists of enormous dynamical nanoparticles, and the spin fields are generated by the first scattering from laser illumination and are probed by the nanoparticles in the diffusion region, resulting in macroscale spin distributions from many incoherent scatterings. This phenomenon is universal and ubiquitous, and it can occur for nanoparticles with different shapes, sizes or refractive indices. The measurement of this spin effect can be developed as a spin-resolved optical means to detect the size, material and other properties of nanoparticles using a simple paraxial optical imaging system. As Brownian motions are widely present, this method may find broad applications in chemistry, biology, micromechanics and materials science. Complex disordered systems offer a plethora of fascinating wave phenomena, and many of them are unexpected. Our study can be an inspiration for discovering similar effects in other wave-based systems for both classical and quantum regimes. One possible direction in the future is to investigate dynamical spin effects using fast optical detecting approaches^{37,38} or, equivalently, by slowing down the Brownian motion via temperature or viscosity control. Moreover, the Brownian system can be composed of engineered nanostructures with customized size and shape. In this sense, the nanoparticles are thermally fluctuating metamolecules, and a Brownian system resembles a liquid metamaterial, enabling exotic light–matter interactions.

Online content

Any methods, additional references, Nature Portfolio reporting summaries, source data, extended data, supplementary information, acknowledgements, peer review information; details of author contributions and competing interests; and statements of data and code availability are available at <https://doi.org/10.1038/s41563-025-02413-5>.

References

- Anderson, P. W. Absence of diffusion in certain random lattices. *Phys. Rev.* **109**, 1492 (1958).
- Segev, M., Silberberg, Y. & Christodoulides, D. N. Anderson localization of light. *Nat. Photonics* **7**, 197–204 (2013).
- Rogers, E. T. et al. A super-oscillatory lens optical microscope for subwavelength imaging. *Nat. Mater.* **11**, 432–435 (2012).
- Patsyk, A., Sivan, U., Segev, M. & Bandres, M. A. Observation of branched flow of light. *Nature* **583**, 60–65 (2020).
- van Tiggelen, B. A. Transverse diffusion of light in Faraday-active media. *Phys. Rev. Lett.* **75**, 422 (1995).
- Hasan, M. Z. & Kane, C. L. Colloquium: topological insulators. *Rev. Mod. Phys.* **82**, 3045–3067 (2010).
- Haldane, F. D. M. Model for a quantum Hall effect without Landau levels: condensed-matter realization of the “parity anomaly”. *Phys. Rev. Lett.* **61**, 2015 (1988).
- Savary, L. & Balents, L. Quantum spin liquids: a review. *Rep. Prog. Phys.* **80**, 016502 (2016).
- Anderson, P. W. The resonating valence bond state in La_2CuO_4 and superconductivity. *science* **235**, 1196–1198 (1987).
- Sinova, J., Valenzuela, S. O., Wunderlich, J., Back, C. & Jungwirth, T. Spin hall effects. *Rev. Mod. Phys.* **87**, 1213–1260 (2015).
- Neugebauer, M., Eismann, J. S., Bauer, T. & Banzer, P. Magnetic and electric transverse spin density of spatially confined light. *Phys. Rev. X* **8**, 021042 (2018).
- Rodríguez-Herrera, O. G., Lara, D., Bliokh, K. Y., Ostrovskaya, E. A. & Dainty, C. Optical nanoprobnging via spin–orbit interaction of light. *Phys. Rev. Lett.* **104**, 253601 (2010).
- Shitrit, N. et al. Spin-optical metamaterial route to spin-controlled photonics. *Science* **340**, 724–726 (2013).
- Rong, K. et al. Photonic Rashba effect from quantum emitters mediated by a Berry-phase defective photonic crystal. *Nat. Nanotechnol.* **15**, 927–933 (2020).
- Onoda, M., Murakami, S. & Nagaosa, N. Hall effect of light. *Phys. Rev. Lett.* **93**, 083901 (2004).
- Bliokh, K. Y., Smirnova, D. & Nori, F. Quantum spin Hall effect of light. *Science* **348**, 1448–1451 (2015).
- Shi, P., Du, L., Li, C., Zayats, A. V. & Yuan, X. Transverse spin dynamics in structured electromagnetic guided waves. *Proc. Natl Acad. Sci. USA* **118**, e2018816118 (2021).
- Van Mechelen, T. & Jacob, Z. Universal spin-momentum locking of evanescent waves. *Optica* **3**, 118–126 (2016).
- Bliokh, K. Y. & Nori, F. Transverse spin of a surface polariton. *Phys. Rev. A* **85**, 061801 (2012).
- Vernon, A. J., Golat, S., Rigouzzo, C., Lim, E. A. & Rodríguez-Fortuño, F. J. A decomposition of light’s spin angular momentum density. *Light Sci. Appl.* **13**, 160 (2024).
- Picardi, M. F., Zayats, A. V. & Rodríguez-Fortuño, F. J. Janus and Huygens dipoles: near-field directionality beyond spin-momentum locking. *Phys. Rev. Lett.* **120**, 117402 (2018).
- Rodríguez-Fortuño, F. J. et al. Near-field interference for the unidirectional excitation of electromagnetic guided modes. *Science* **340**, 328–330 (2013).
- Vernon, A. J., Kille, A., Rodríguez-Fortuño, F. J. & Afanasev, A. Non-diffracting polarization features around far-field zeros of electromagnetic radiation. *Optica* **11**, 120–127 (2024).
- Neugebauer, M., Banzer, P. & Nechayev, S. Emission of circularly polarized light by a linear dipole. *Sci. Adv.* **5**, eaav7588 (2019).
- Bliokh, K. Y., Rodríguez-Fortuño, F. J., Nori, F. & Zayats, A. V. Spin-orbit interactions of light. *Nat. Photonics* **9**, 796–808 (2015).
- Bardon-Brun, T., Delande, D. & Cherroret, N. Spin Hall effect of light in a random medium. *Phys. Rev. Lett.* **123**, 043901 (2019).
- Hosten, O. & Kwiat, P. Observation of the spin Hall effect of light via weak measurements. *Science* **319**, 787–790 (2008).
- Bomzon, Z. E., Biener, G., Kleiner, V. & Hasman, E. Space-variant Pancharatnam–Berry phase optical elements with computer-generated subwavelength gratings. *Opt. Lett.* **27**, 1141–1143 (2002).
- Kim, M., Lee, D., Yang, Y., Kim, Y. & Rho, J. Reaching the highest efficiency of spin Hall effect of light in the near-infrared using all-dielectric metasurfaces. *Nat. Commun.* **13**, 2036 (2022).
- Yin, X., Ye, Z., Rho, J., Wang, Y. & Zhang, X. Photonic spin Hall effect at metasurfaces. *Science* **339**, 1405–1407 (2013).
- Maguid, E. et al. Disorder-induced optical transition from spin Hall to random Rashba effect. *Science* **358**, 1411–1415 (2017).
- Wang, B., Rong, K., Maguid, E., Kleiner, V. & Hasman, E. Probing nanoscale fluctuation of ferromagnetic meta-atoms with a stochastic photonic spin Hall effect. *Nat. Nanotechnol.* **15**, 450–456 (2020).
- Einstein, A. Über die von der molekularkinetischen Theorie der Wärme geforderte Bewegung von in ruhenden Flüssigkeiten suspendierten Teilchen. *Ann. Phys.* **322**, 549–560 (1905).
- Berne, B. J. & Pecora, R. *Dynamic Light Scattering: With Applications to Chemistry, Biology, and Physics* (Courier Corporation, 2000).
- Aiello, A., Banzer, P., Neugebauer, M. & Leuchs, G. From transverse angular momentum to photonic wheels. *Nat. Photonics* **9**, 789–795 (2015).
- Eismann, J. et al. Transverse spinning of unpolarized light. *Nat. Photonics* **15**, 156–161 (2021).

37. Huang, R. et al. Direct observation of the full transition from ballistic to diffusive Brownian motion in a liquid. *Nat. Phys.* **7**, 576–580 (2011).
38. Kheifets, S., Simha, A., Melin, K., Li, T. & Raizen, M. G. Observation of Brownian motion in liquids at short times: instantaneous velocity and memory loss. *Science* **343**, 1493–1496 (2014).

Publisher's note Springer Nature remains neutral with regard to jurisdictional claims in published maps and institutional affiliations.

Springer Nature or its licensor (e.g. a society or other partner) holds exclusive rights to this article under a publishing agreement with the author(s) or other rightsholder(s); author self-archiving of the accepted manuscript version of this article is solely governed by the terms of such publishing agreement and applicable law.

© The Author(s), under exclusive licence to Springer Nature Limited 2025

Methods

The theory of the Brownian spin-locking effect

To evaluate the observed phenomena in a macroscale scattering system, we established a scattering theory that simplifies the complex scattering into two essential physical processes (Supplementary Fig. 18). The simulation parameters are set to match the experimental conditions, in which a laser beam with a diameter of approximately 2 mm is incident on a 1 cm × 1 cm glass container. In the laser illumination region, 30 nanoparticles are distributed along the z axis within the range $z \in [0, 1 \text{ cm}]$, at $x = 0$ and $y = 0$. The incident laser light field, \mathbf{E}_0 , excites one of the nanoparticles in the illumination region, resulting in a radiation source $\mathbf{E}_b = \mathbf{M} \times \mathbf{E}_0$. Here, \mathbf{M} represents the Mie scattering matrix, and \mathbf{E}_b propagates in space following the exact solution. In the diffusion region, particles are located within the spatial bounds $x \in [1 \text{ mm}, 5 \text{ mm}]$, $y \in [2.5 \text{ mm}, 2.5 \text{ mm}]$ and $z \in [0 \text{ mm}, 5 \text{ mm}]$. These nanoparticles in the diffusion region \mathbf{r}_d are similarly excited by \mathbf{E}_b , resulting in $\mathbf{E}_d = \mathbf{M} \times \mathbf{E}_b$. We calculated the superposition of the fields \mathbf{E}_d from many nanoparticles at different \mathbf{r}_b . In the case of incoherent scattering, we project the field $\mathbf{E}_d(\mathbf{r}')$ onto the spin-up and spin-down states, and obtain $I_R(\mathbf{r}')$ and $I_L(\mathbf{r}')$, respectively. The intensities are summed over all nanoparticles, $I_{R,L}(\mathbf{r}_d) = \sum_{\mathbf{r}_b} I_{R,L}(\mathbf{r}_d - \mathbf{r}_b)$. The macroscale spin effect is then shown by calculating the spatial distribution of the difference between $I_R(\mathbf{r}_d)$ and $I_L(\mathbf{r}_d)$. By configuring the nanoparticle diameter and the polarization state of the incident light, simulation results can be obtained for different cases, including linearly polarized incidence, circularly polarized incidence and nanoparticles of varying materials and sizes.

Characterizing the spin-locking effect with varying acquisition times

To detect the real-time intensities of opposite spin polarizations, a polarized grating is inserted in the set-up, as shown in Fig. 3a. This polarized grating (ZGS25-700-10-SP241211) works similarly to a geometric phase metasurface, which can split the spin-up and spin-down components of an image into different directions. This allows us to measure the spin of scattered light on a very short timescale (~0.4 ms). The samples are contained in a 2 mm × 1 cm glass container (Fig. 3a), consisting of spherical Fe_3O_4 with $\langle D \rangle = 470 \text{ nm}$ or SiO_2 nanospheres with $\langle D \rangle = 1,690 \text{ nm}$ suspended in water (Fig. 3b). The camera (Basler, acA720-520uc) is configured to capture about 2,000 frames per second. An x -polarized plane wave laser (wavelength 639 nm, beam width ~2 mm) impinges on the samples at normal incidence. For each measurement, the camera continually captures images for 1 s. We select diffusion regions on the images and use $s_x = (I_R - I_L)/(I_R + I_L)$ to calculate the real-time (resolution ~0.4 ms) spin distributions. As shown in Fig. 3a, by summing the recorded intensity frames over different time durations, the intensities of opposite spin polarizations with various t_{exp} can be reconstructed. The spin probability distributions in the upper and lower diffusion regions are analysed, enabling the evolution of the fluctuation width (Δs_x) over time. The second-order autocorrelation function g_2 is measured using a DLS method (Supplementary Section 11).

Polarization characterization

To obtain the DoP of the observed scattered light, we conduct experiments to measure the Stokes parameters s_0, s_1, s_2 and s_3 under different linear polarization states of the incident light. The Stokes parameters are calculated as

$$s_0 = (I_{0^\circ} + I_{90^\circ} + I_{45^\circ} + I_{135^\circ} + I_R + I_L)/3,$$

$$s_1 = (I_{0^\circ} - I_{90^\circ})/s_0,$$

$$s_2 = (I_{45^\circ} - I_{135^\circ})/s_0,$$

$$s_3 = (I_R - I_L)/s_0.$$

Here, $I_{0^\circ}, I_{90^\circ}, I_{45^\circ}$ and I_{135° represent the intensities of the scattered light after passing through a linear polarizer oriented horizontally, vertically, 45° and 135° , respectively, which are measured after the polarizer. The intensities I_R and I_L are measured by inserting a quarter-wave plate with its fast axis aligned with the z axis before the linear polarizer and recording the scattering intensities with the polarizer set to 135° and 45° . The DoP of the observed scattered light is calculated as

$$\text{DoP} = \sqrt{s_1^2 + s_2^2 + s_3^2}.$$

The obtained intensity s_0 and DoP are averaged along the z axis to obtain their y -dependent behaviour (Fig. 4b). The incident laser power is ~19 mW, and the exposure time of the camera is 600 μs . The results for unpolarized light are obtained by summing the intensities of these measurements from different polarization states.

Data availability

Source data are provided with this paper. Additional data supporting the conclusions of this study are available from the corresponding author upon request.

Acknowledgements

We thank X. Cao for helping us with sample preparation, and useful discussions with Y. Pan at the early stage of this work. This work is supported by National Key Research and Development Program of China (grant no. 2022YFA1205101), National Science Foundation of China (grant nos. 12274296 and 12192252), Shanghai International Cooperation Program for Science and Technology (grant no. 22520714300) and Shanghai Jiao Tong University 2030 Initiative. B.W. is sponsored by Yangyang Development Fund. E.H. acknowledges financial support from the Israel Science Foundation (grant no. 1170/20).

Author contributions

E.H., B.W. and X.C. supervised this work. B.W. initialized theory and experiment, observed the phenomena and wrote the manuscript. X.Z. systematically performed experimental work, theory and figure preparation. P.C. contributed importantly in Mie theory analysis and assisted in experimental characterization. M.L. performed g_2 and SEM measurement. Y.S. assisted in manuscript revision. B.W., X.Z., P.C. and M.L. prepared the supplementary material. E.H. and X.C. contributed to discussions at all stages of this work and revised the manuscript.

Competing interests

The authors declare no competing interests.

Additional information

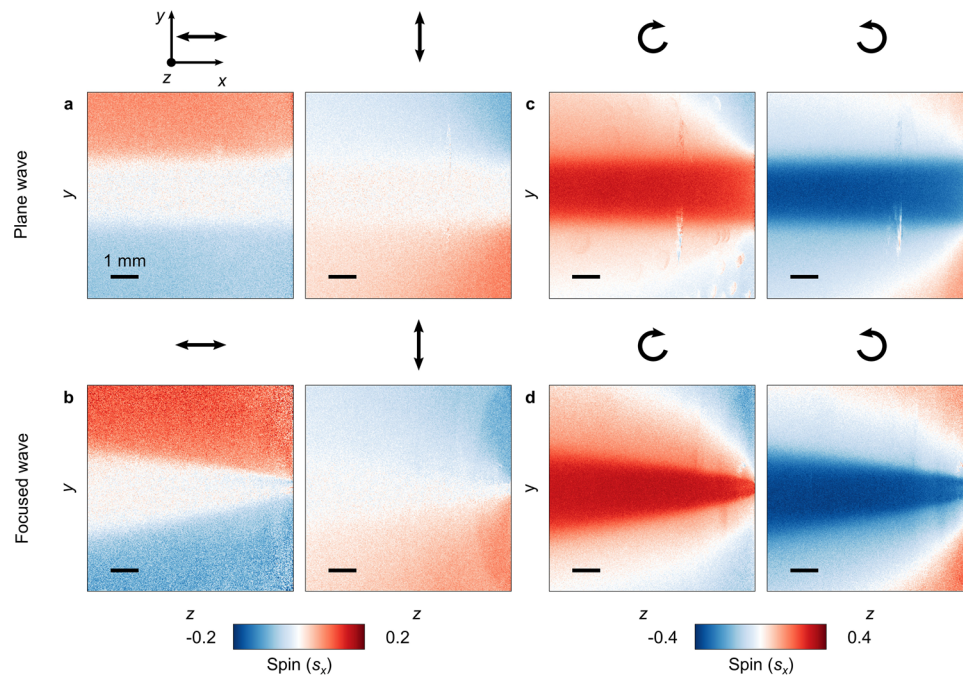
Extended data is available for this paper at <https://doi.org/10.1038/s41563-025-02413-5>.

Supplementary information The online version contains supplementary material available at <https://doi.org/10.1038/s41563-025-02413-5>.

Correspondence and requests for materials should be addressed to Erez Hasman, Bo Wang or Xianfeng Chen.

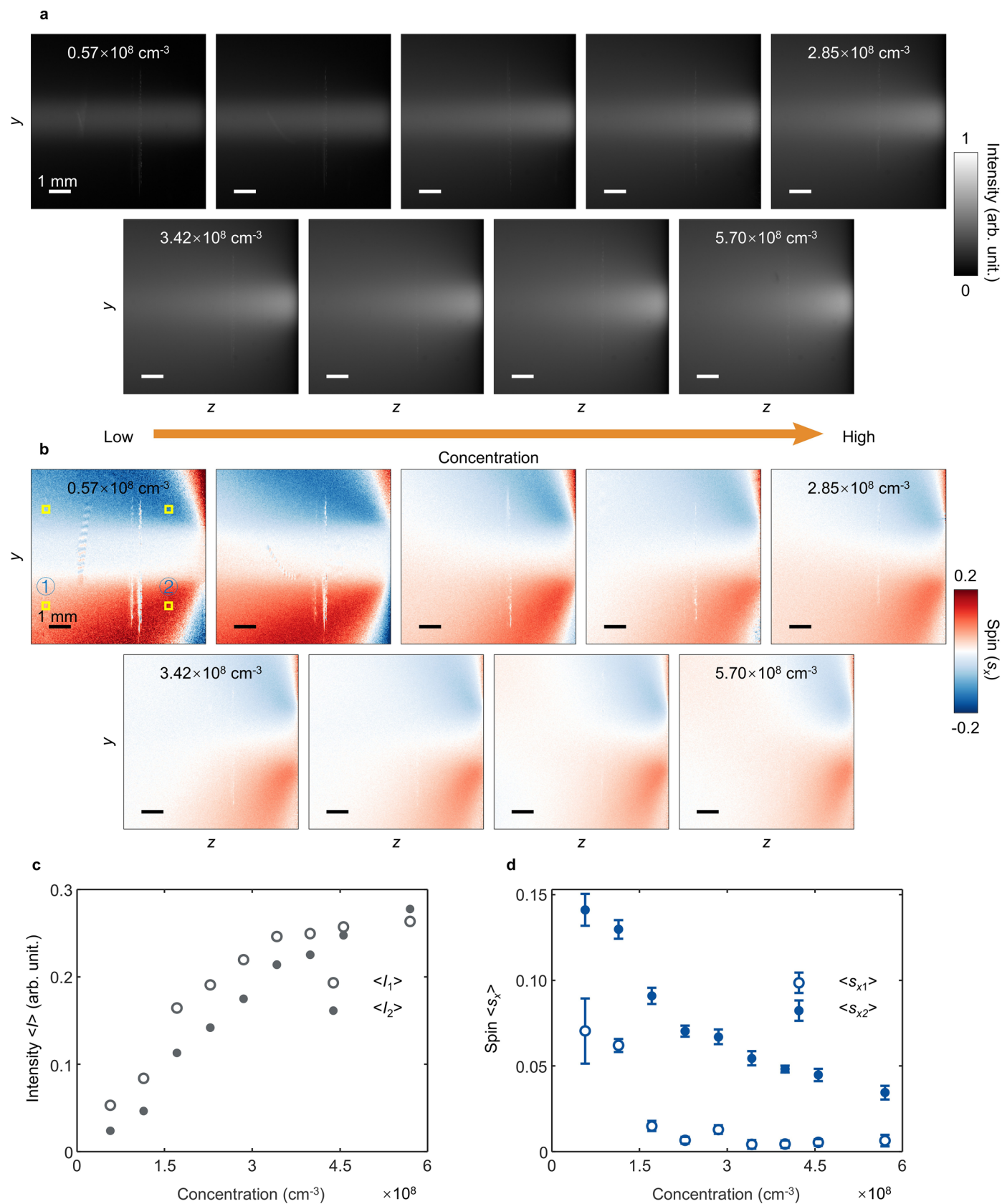
Peer review information *Nature Materials* thanks Francisco Rodríguez Fortuño and the other, anonymous, reviewer(s) for their contribution to the peer review of this work.

Reprints and permissions information is available at www.nature.com/reprints.



Extended Data Fig. 1 | Observations for different laser beam waists and polarizations. (a) and (c): plane-wave illumination (Gaussian beam waist ~ 2 mm); (a) is x - and y -polarized, and (c) is left- and right-handed circularly polarized. (b) and (d): focused-beam illumination (focused beam waist < 0.5 mm); (b) is x - and y -polarized, and (d) is left- and right-handed circularly polarized. When

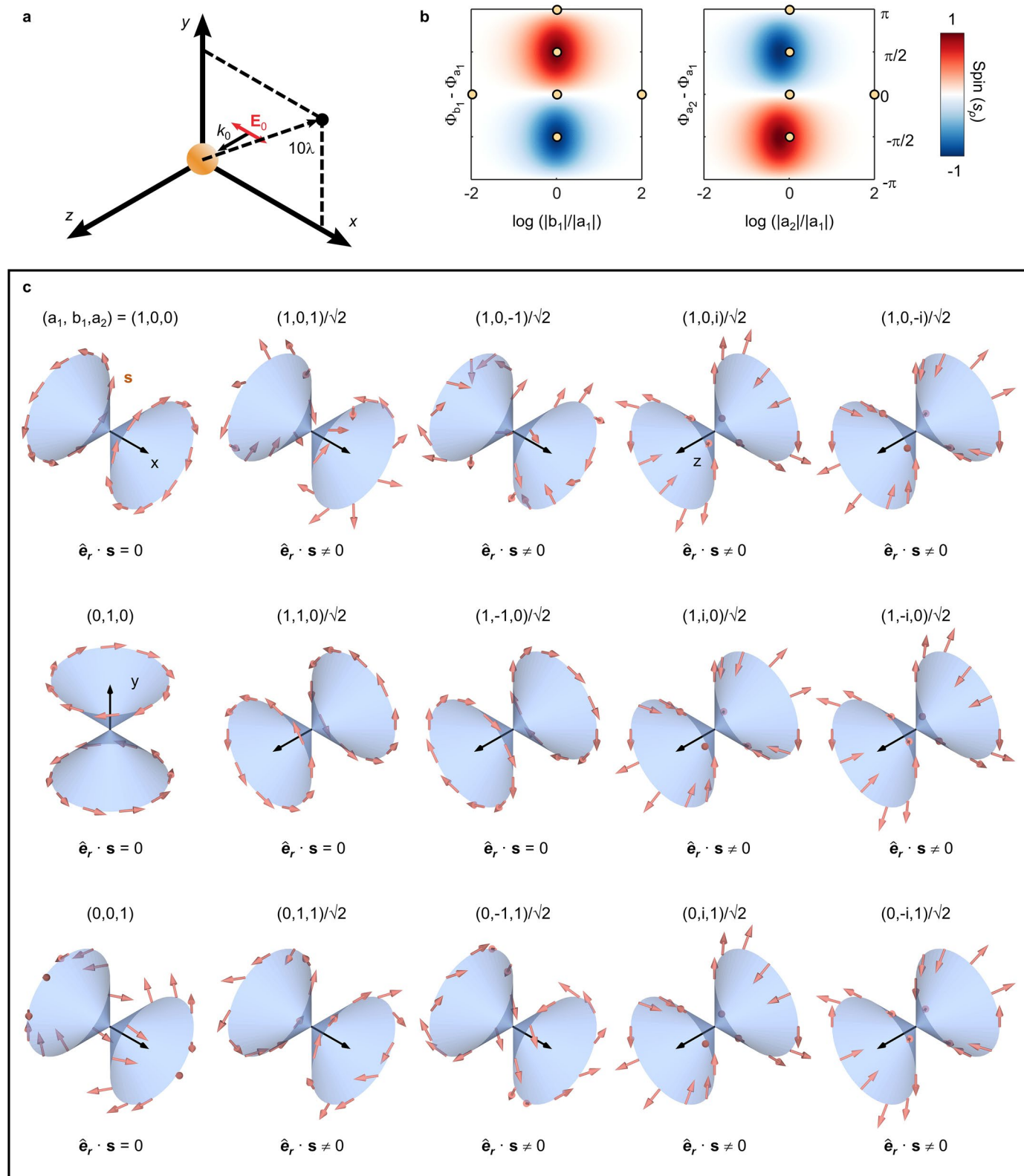
the incident light is linearly polarized (along x or y), the spin distributions under both plane wave and focused beam illumination are very similar. Under circular polarizations, the spin values are stronger in the illumination region but weaker in the diffusion region.



Extended Data Fig. 2 | See next page for caption.

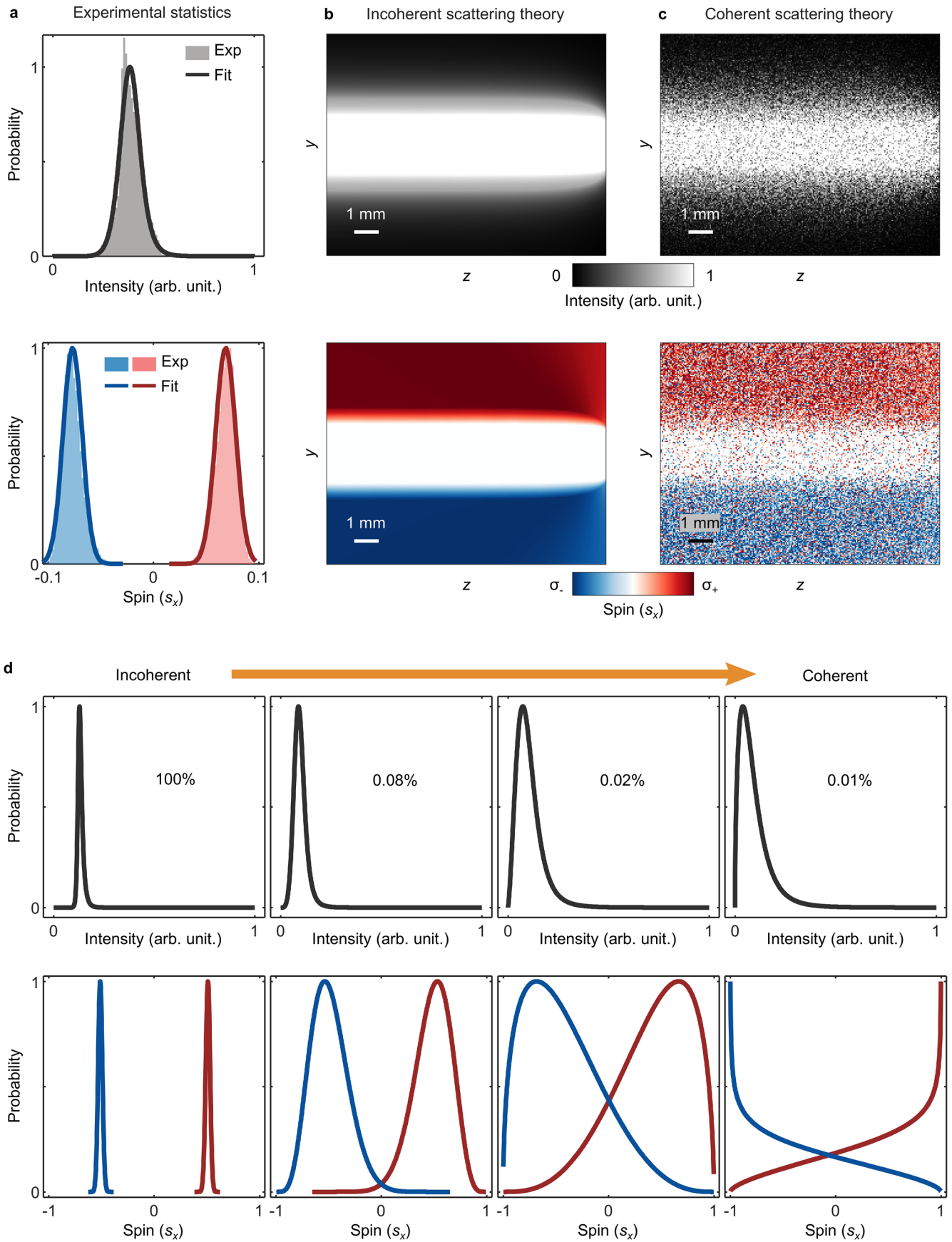
Extended Data Fig. 2 | Experimentally observed Brownian spin-locking effect for different Fe_3O_4 nanoparticle concentrations. Normalized light intensity distributions (a) and s_x distributions (b) for various concentrations of Fe_3O_4 nanoparticles in water. ① and ② (yellow boxes) denote the analysis regions used to extract the light intensity and s_x values in (c) and (d). The two upper boxes represent regions symmetric to ① and ② with respect to the laser beam. The laser is incident from the right side of the images. (c) Variation of normalized light intensity with particle concentration. $\langle I_1 \rangle$ ($\langle I_2 \rangle$) represents the average light intensity in region ① (②). (d) Variation of $\langle s_x \rangle$ with particle concentration. $\langle s_{x1} \rangle$ ($\langle s_{x2} \rangle$) represents the average absolute value of s_x in region ① (②). As the

concentration increases, the spin effect becomes weaker, although its spatial distribution remains similar. While the intensity evolution in both regions (① and ②) is comparable across the concentration range, the spin distributions differ significantly. Specifically, when the concentration of nanoparticles is approximately $2.28 \times 10^8 \text{ cm}^{-3}$, the statistically averaged spin at region ①, $\langle s_{x1} \rangle$, approaches 0, while $\langle s_{x2} \rangle$ is about 0.09. Notably, the s_x distribution near region ② persists over a wide range of concentrations, indicating the robustness of the Brownian spin-locking effect across single and multiple scattering regimes. Data are presented as mean \pm s.d. (technical replicates, $n = 10$).



Extended Data Fig. 3 | Spin angular momentum properties of the scattering field for different combinations of multipoles. (a) Schematic of Mie scattering. The location of the analytical point (black dot) in the figure is $(5\sqrt{2}\lambda, 5\sqrt{2}\lambda, 0)$. (b) Phase diagram of s_p at the black dot in (a) with respect to Mie scattering coefficients. s_p represents the radial component of the spin angular momentum density in the xy plane. Φ_{a_1} , Φ_{b_1} , Φ_{a_2} represent the phases of a_1 , b_1 , a_2 , respectively. The spin is strong if there is a $\pm\pi/2$ phase difference between the two coupled modes, and disappears if the phase difference approaches 0 or π . (c) Spin angular momentum distribution of the Mie scattering field under different

combinations of Mie coefficients. The short arrows (orange arrows) represent the spin angular momentum. These scattering cases are divided into three different types. One, for instance, the electric dipole, represents topological-insulator-like spin textures with two orbital spin distributions perpendicular to the radiation cones $(a_1, b_1, a_2 = 1, 0, 0)$. This is a typical transverse spin. For the Janus dipole, the spins are parallel to the radiation cones $(a_1, b_1, a_2 = 1, i, 0)$, that is, longitudinal spin. In general, the spin from scattering is neither perpendicular nor parallel to the kinetic momentum.



Extended Data Fig. 4 | See next page for caption.

Extended Data Fig. 4 | Statistical properties of the Brownian spin-locking effect and incoherent scattering theory. (a) The histograms are experimentally observed statistical distributions of the spatial intensity (upper panel) and spin (lower panel), which are obtained from the diffusion regions of Figs. 1d and 1e, respectively. The solid curves are fitted using a Burr distribution for the intensity and a Beta distribution for the spin. (b) The calculated spatial distributions of the normalized intensity and spin from the incoherent scattering theory. (c) The

calculated spatial distributions of the normalized intensity and spin from the coherent scattering theory. (d) The theoretical evolution of the intensity and spin distributions by changing m/N from 100% (incoherent) to 0.01% (coherent). As the degree of coherence increases, the spin distributions become wider with enhanced skewness, corresponding to increased spin fluctuations that reduce the spin-locking phenomenon.